A Circularly Polarized Sub-Terahertz Antenna With Low-Profile and High-Gain for 6G Wireless Communication Systems

BASEM AQLAN[1,2], **MOHAMED HIMDI**[2], **HAMSAKUTTY VETTIKALLADI**[1], **AND LAURENT LE-COQ**[2]

[1]Department of Electrical Engineering, King Saud University, Riyadh 11421, Saudi Arabia
[2]Institut d'Electronique et des Technologies du numeRique (IETR), University of Rennes 1, 35000 Rennes, France

Corresponding author: Basem Aqlan (baqlan@ksu.edu.sa)

ABSTRACT A low-profile high-gain fully-metallic circularly polarized (CP) Fabry–Perot cavity (FPC) antenna using laser cutting technology at 300 GHz is presented. The CP-FPC antenna consists of seven metallic layers arranged from the bottom to the top: a ground layer, an integrated stepped horn element (three layers), a coupling slots layer, a cavity layer, and an aperture-frequency selective surface (FSS) layer. The high gain and self-generation of circular polarization are made by using this FSS layer by introducing periodic hexagonal –shaped aperture in a thin metallic layer. The aperture–FSS layer is used to excite two orthogonal modes of equal in magnitude and in phase quadrature, thus obtaining the RHCP radiation. The proposed CP-FPC antenna structure achieves a measured peak RHCP gain of 16.5 dBic at 292 GHz. The antenna achieves a measured impedance bandwidth of 281– 305 GHz for the reflection coefficient less than -10 dB. The axial ratio (AR) bandwidth AR $\leq$ 3 dB is 5.12 GHz from 292.8 to 297.92 GHz. The fabricated CP-FPC antenna uses a low-cost laser cutting technique with a low-profile and an area of 2.6 mm $\times$ 2.6 mm $\times$ 1.24 mm. The experimental results confirm a good agreement between the simulation and the measurements.

INDEX TERMS Axial ratio (AR), circularly polarized (CP), Fabry–Perot cavity (FPC) antenna, frequency selective surface (FSS), high-gain, laser-cutting technology, low-profile, low-cost, metallic layers, sub-terahertz (THz).

I. INTRODUCTION

Recently, the global wireless data traffic has been exponentially increasing along with the growth of applications that require data rates of several tens of Gbps. The increase in the data rate provided by every new generation of cellular networks is insufficient to the annual growth of demand. The significant rapid growth of wireless utilization has driven researchers to investigate appropriate regions in the radio spectrum to fulfill this demand [1]. The terahertz (THz) frequency band (0.1–10 THz) is a slice of the electromagnetic (EM) spectrum between the millimeter and the infrared regions. Its innovative properties and inherently large bandwidth are expected to be used for future promising applications. The sub-THz frequency band (0.1–1 THz) offers a spectrum with a high data rate, wide bandwidth, and lower rain and fog atmospheric attenuation [2]. This frequency band is intended to serve terabits per second (Tbps) wireless communication for the sixth generation (6G) mobile network [3]. The IEEE standard 802.15.3d, published in October 2017, defines the use of the sub-THz frequency range 252–325 GHz (300-GHz band) as the high-data-rate wireless communication channels that enables up to 100 Gbps [4]. Generally, the antenna is an indispensable component of any THz wireless communication systems along with active components and associate technologies. In other words, the performance of the antenna directly affects the communication quality of the entire system.

One of THz-band frequencies' main challenges is a very high path loss, resulting in a major constraint on

The associate editor coordinating the review of this manuscript and approving it for publication was Sudipta Chattopadhyay.

communication distances. At THz frequencies, the need for high-gain antennas is very important to overcome high atmospheric absorption and high path loss at these frequencies, which will affect the wireless link budget. Horn antennas and reflector-based antennas have been proposed at THz frequencies [5]–[7] because of their good radiation performance; however, they are bulky in size and have a complex structure, especially when integrating them with other active compact components. Thus, planar antennas are required for compact-integrated systems at low THz frequencies. Recently, the Fabry–Perot cavity (FPC) antennas were developed to realize high directivity and improved bandwidth. Having a single feeding source, FPC antennas offer a promising alternative to slotted waveguide array antennas and standard antenna arrays. At higher frequencies, linearly polarized FPC antennas also offer significant advantages in a simple configuration, low fabrication complexity, high radiation efficiency, and good radiation pattern performance [8]–[10]. Moreover, circularly polarized (CP) antennas are required for wireless communication systems because of their ability to avoid multipath fading, mismatch the polarization (alignment issue), and enhance the channel capacity. Therefore, developing front-end components with the focusing of CP sub-THz antennas is important. Recently, some applied sub-THz antennas with circular polarization studies were also shown in the literature. As reported in [11], [12], hexagonal waveguide-based horn antenna operates at 110 GHz and 0.3 THz for conical horn antenna, using wire electrical discharge machining (EDM) technology. For these horn antennas, it is difficult to process the integration with planar circuits and miniaturization. Other researches published in [13, 14] presented discrete dielectric lens fed by a standard linearly polarized pyramidal horn working at 0.3 THz, using a 3D printing technology. These lenses are highly directive antennas that have a large profile of several wavelengths, which can be a problem at a sub-THz band (300 GHz) particularly in the case of compact-integrated systems. Antipodal curvedly tapered slot and double-fan-shaped slot antennas operating at 0.5 THz are described in [15], [16]. These planar antennas are readily compatible with micromachining techniques, leading to compact-integrated systems at low THz frequencies. Normally, at microwave band, a patch antenna is used as the radiating element; however, because of the excited surface wave of the relatively thick substrate, it is lossy and narrow-band at THz band. Use of metallic structure can alleviate this problem.

In this work we present a sub-THz antenna fabricated using a laser-cutting technology. The experimental prototype reported here represents the first fully metallic CP-FPC antenna enabled by laser-cutting in the sub-THz range. Using laser-cutting metal brass, we present the simplified technology procedure at 300 GHz; with a low-cost fabrication process. This laser cutting technology works by directly cutting the brass metal layers, without the need of a mask and a metallization process, which ease the fabrication. All brass metals layers are simply stacked by using

four plastic screws. This direct-mount procedure is easier to alternative setups of silicon-micromachining which needs a bonding alignment method [17], and is expensive.

Section II describes the antenna architecture and main design rules. To validate the proposed concept, we presented in Sections III and IV the fabricated prototypes and measurement results. Finally, Section V concludes this research.

II. ANTENNA CONFIGURATION AND DESIGN
A. UNIT CELL MODEL (HEXAGONAL APERTURE ELEMENT)
The design model of a unit cell for aperture type-FSS layer is studied using periodic analysis, since this model assume the transverse extent of hexagonal radiating aperture unit cell structure and is theoretically infinite. Periodic boundary analysis is performed using the frequency-domain solver of CST Microwave Studio. Furthermore, this model assumes that the FSS layer is illuminated by a normally incident plane wave, i.e., that the propagation vector is normal to the plane of the FSS layer. We can achieve a high gain antenna when the reflection coefficient magnitude of the unit cell is high [8]. Furthermore, to improve the antenna bandwidth the reflection coefficient phase of the unit cell should vary slowly with frequency. Thus, the proposed unit cell of hexagonal radiating apertures FSS layer achieves its requirements. The hexagonal aperture is used to excite two orthogonal modes with an equal magnitude and a 90° phase difference between them, thus inducing CP current and radiating CP waves.

The aperture-type FSS acts as a partially reflective surface (PR), which function as high-gain antennas [8], [18], where a hexagonal aperture element has been chosen as FSS unit cell for the design. The aperture-FSS layer is placed at a half-wavelength height above the ground plane to form a one-dimensional cavity, leading to a high directive beam radiation, which is generally explained by the ray-tracing or leaky-wave approach [18], [19].

Fig. 1 demonstrates the geometry of the proposed hexagonal radiating aperture unit cell. It is found that the periodicity of the unit cell $p = 0.48 \lambda_0$, the unit cell has two symmetrically isosceles triangle chamfers, $c_t = 0.14 \lambda_0$, and the thickness of radiating aperture, $t_{FSS} = 0.1 \lambda_0$, where λ_0 is the operation frequency at 300 GHz.

B. CIRCULARLY POLARIZED FABRY-PEROT CAVITY ANTENNA
Fig. 2(a) shows the 3D view of the FPC antenna with aperture type-FSS layer at 300 GHz. The proposed antenna comprises of seven metallic layers: ground layer, integrated stepped horn layers (three layers), coupling layer, cavity layer, and FSS layer. A slot antenna is engraved on the ground layer (layer A) with a thickness of $t_1 = 0.1 \lambda_0$.

The standard WM-864 rectangular waveguide (864 μm × 432 μm) feed is directly connected to layer A at the backside. The length of the slot is usually chosen to be a half-wavelength. This single waveguide-fed slot acts as the primary feed antenna. Layer A is the coupling slot element
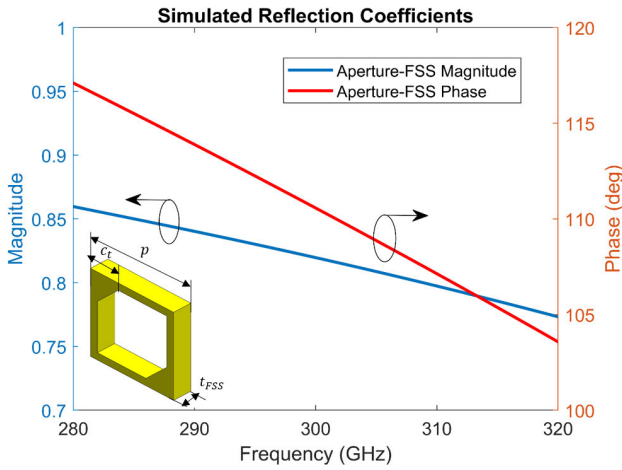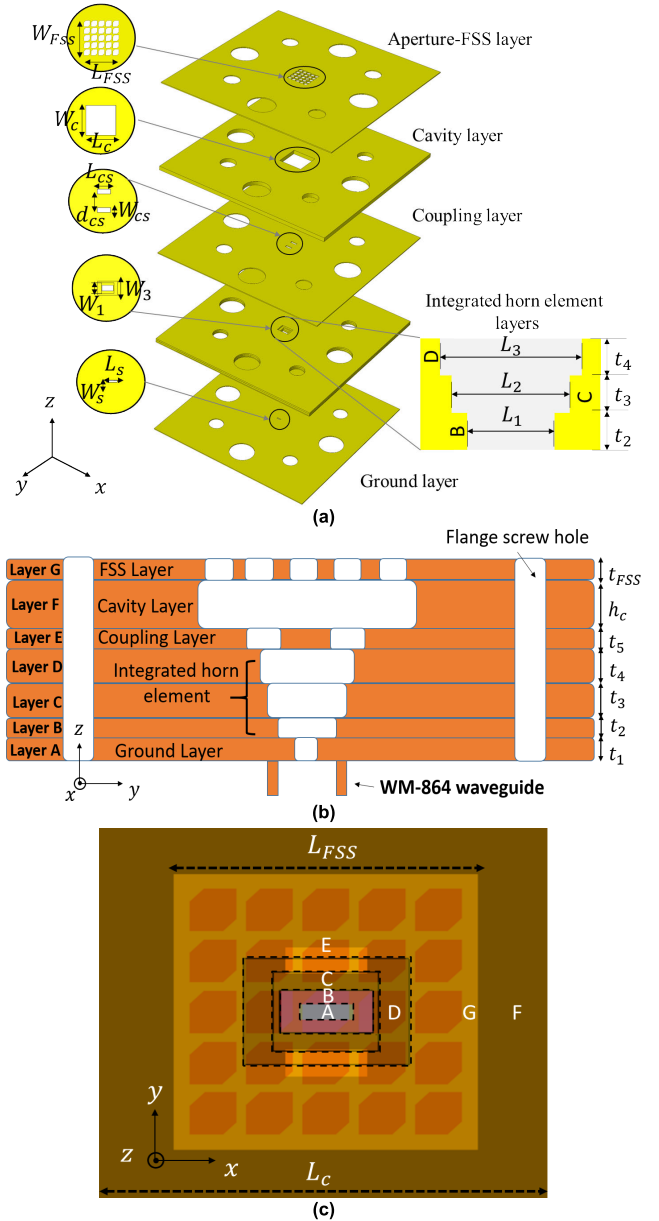
FIGURE 1. Simulated complex reflection coefficient of the proposed aperture–FSS unit cell.

FIGURE 2. Configuration: (a) exploded view of the proposed antenna, (b) cross-section view, and (c) top view.

widely used; however, the resonant element may restrict the realization of the wideband impedance matching. Inspired by the conventional broadband horn antenna, the coupling slot size can progressively increase (B, C and D layers) and realize the wideband impedance matching from the exciting source. The conventional horn antenna design is transformed into an integrated step-profiled horn. To construct the integrated step-profiled horn element, we used layers B, C, and D, as shown in Fig. 2(b), formed by three rectangular aperture shapes of metallic layers.

To improve the antenna impedance matching, we used the horn element. A coupling layer (layer E) consisting of two parallel slots is used to broaden the single-slot feed's impedance matching bandwidth in the ground layer. Cavity layer (layer F) is used to support the FSS layer, which is the distance to achieve resonance condition of Fabry–Pérot by using Equation (1-2). The FSS layer is realized by perforated grids of hexagonal radiating apertures made by cutting through a metallic layer of finite thickness of 0.1 mm, supported by a metallic cavity layer, forming an air cavity with the metallic coupling layer.

For fabrication, we integrate the standard UG-387/U waveguide flange into the antenna design. The side view of the FPC antenna with aperture type-FSS layer is shown in Fig. 2b. There is a coupling between the base antenna (A–E layers) and the FSS layer that affects the antenna's performance in terms of S11, gain, and efficiency. The EM waves radiated from the base antenna impinge on the FSS layer, which forces the distribution of EM waves in space and controls the phase.

The apertures of the FSS gets excited, and multiple reflections and transmissions happen inside the cavity layer; finally, the wave leakage outside of the cavity from the FSS layer and this coherent wave leakage makes the antenna structure become high-gain, affecting the performance of the antenna. The reflection coefficient phase of the whole proposed antenna in Fig. 2(a) is $2\pi N$ as explained in Equation (1), which is calculated by using the simple well-known

ray-tracing formula [8], [20].

$$\varphi_{FSS}(f_0) + \varphi_{Co}(f_0) - 2\beta h_c = 2\pi N; \quad N = 0.1.2.\ldots \quad (1)$$

where N is the order of resonant mode, $\varphi_{FSS}(f_0)$ and $\varphi_{Co}(f_0)$ are the reflection phases of the FSS and the coupling layers, respectively, β is the propagation constant, and h_c is the cavity thickness. The resonance condition takes place at the boresight angle ($\theta = 0°$), and the resonance frequency f_0 can be obtained from the following equation:

$$h_c = \frac{c}{4\pi f_0}[\varphi_{FSS}(f_0) + \varphi_{Co}(f_0) - 2\pi N] \quad (2)$$

From the above analysis, it is clear that the order of resonant mode N usually is equal to zero ($N = 0$) to realize

TABLE 1. Antenna deigns parameters (mm).

Layers	Param.	Value	Param.	Value	Param.	Value
Ground	t_1	0.1	L_s	0.46	w_s	0.1
Integrated horn element	t_2	0.1	L_1	0.8	w_1	0.4
	t_3	0.2	L_2	0.9	w_2	0.75
	t_4	0.2	L_3	1.42	w_3	1
Coupling	t_5	0.1	L_{cs}	0.7	w_{cs}	0.25
Cavity	h_c	0.44	L_c	2.6	w_c	2.6
Aperture-FSS	t_{FSS}	0.1	L_{FSS}	2.32	w_{FSS}	2.32
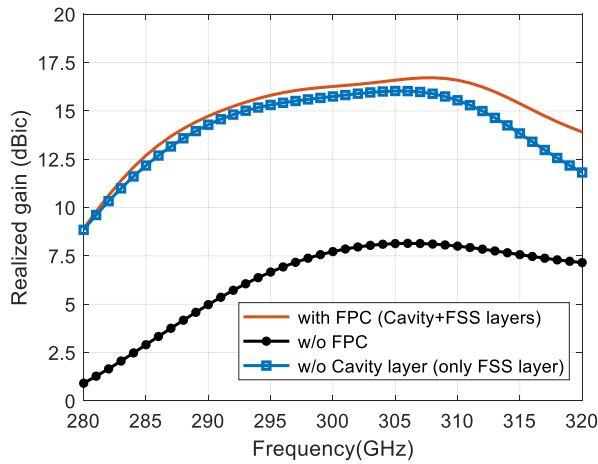
FIGURE 3. Simulated antenna gains with different configuration.

FIGURE 4. Simulated axial ratio, and realized gain versus frequency.
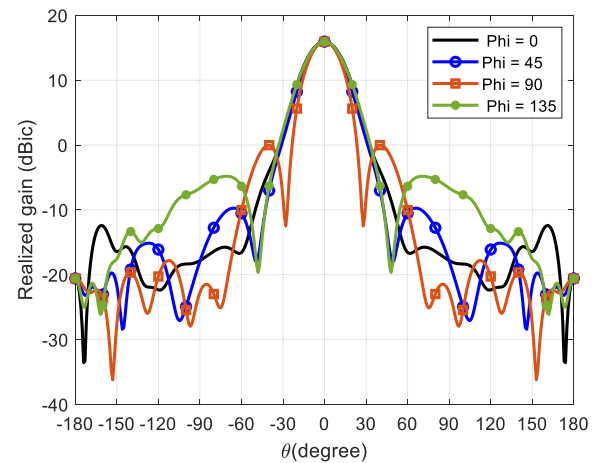
FIGURE 5. Simulated radiation patterns at 296 GHz.

low-profile performance. For a perfect metallic coupling layer and FSS layer, their reflection phase $\varphi_{Co}(f_0)$ and $\varphi_{FSS}(f_0)$ are a multiple of π, provided that the resonance height h_c is approximately $\lambda_0/2$. The 2D top view of the 5×5 element subarray of the hexagonal radiating apertures truncated the corners is depicted in Fig. 2(c). The FSS layer, consisting of an array of hexagonal radiating apertures, is designed for the self-generation of CP waves. The block structure's size, which does not greatly influence the characteristics of the proposed antenna, is set as 20 mm $\times$ 20 mm according to the standard WM-864 waveguide flange size, including alignment and screws holes. The optimized design parameters of the proposed CP-FPC antenna are shown in Table 1.

The simulated realized gain between the antenna with and without FSS layer is shown in Fig. 3. As can be seen, after adding the FSS layer, the gain is significant increased by an average of 7 dB over the whole frequency band, the largest gain difference of 9.3 dB occurs at 290 GHz. Moreover, the antenna gain is again increased by approximately 0.4-2 dB, by the addition of cavity layer, as shown in Fig. 3.

Fig. 4 illustrates optimization in terms of axial ratio (AR) and gain performances of five different apertures–FSS sizes, keeping the same periodicity and dimensions of the aperture unit-cell (due to the reasons explained in Section II.A). The optimum aperture-FSS size in term of the AR and gain is 5×5, which corresponds to lateral size of 2.32 $\lambda_0 \times$ 2.32 λ_0 at 300 GHz. This size was chosen to give the best AR value
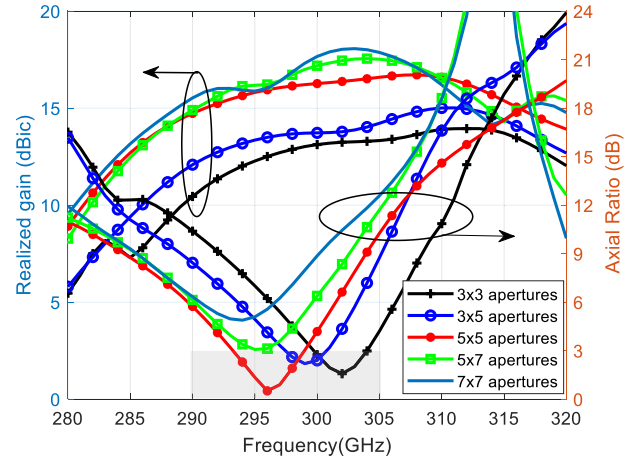
of 0.51 dB, obtained at 296 GHz. The peak realized gain of 16.7 dBic is obtained at 307 GHz.

Fig. 5 shows the simulated right-hand circular polarized (RHCP) realized-gain radiation patterns of the antenna at 296 GHz in four azimuthal cut planes. They are approximately identical, with sidelobes lower than 16 dB. The maximum RHCP gain of 16 dBic is predicted with a 3-dB radiation beamwidth of 26.4° at 296 GHz.

Fig. 6 shows the antenna polarization performance: AR versus the elevation angle (θ) at the frequency of 296 GHz. The best AR is 0.51 dB at broadside direction and the predicted 3-dB AR beamwidth is more than $\pm17.3°$, within the 3-dB radiated beamwidth of 26.4°, indicating that the antenna is indeed radiating most of the energy in circular polarization.

Fig. 7 shows the electric-field distributions in the E-plane cut inside the proposed antenna at 296 GHz, which displays the procedure of the slot coupling EM energies from feed standard WM-864 waveguide to free space.

Fig. 8 illustrates the simulated reflection coefficient (S11) and the realized RHCP gain of the proposed antenna. The reflection coefficient impedance bandwidth <-10 dB is
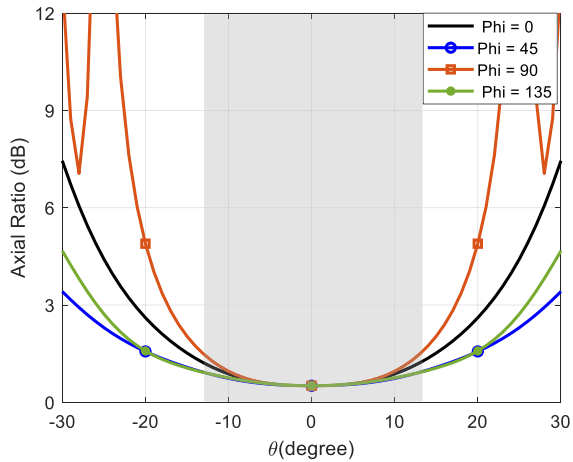
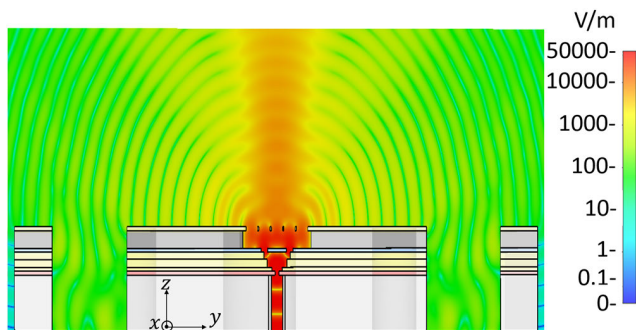FIGURE 6. Simulated angular variation of axial ratio at 296 GHz.

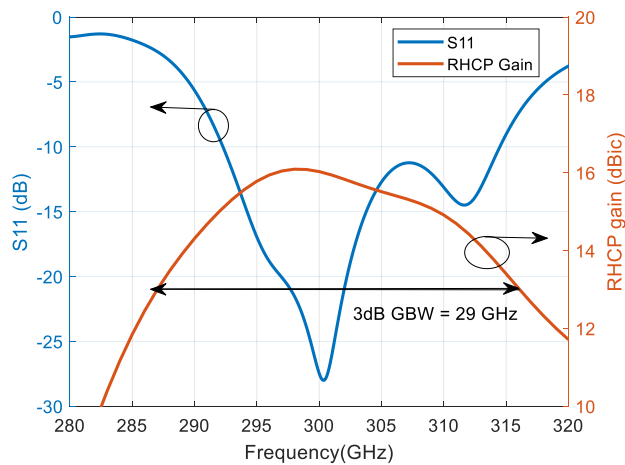FIGURE 7. The E-field distribution in the E-plane cut inside the proposed antenna at 296 GHz.

FIGURE 8. The simulated reflection coefficient (S11) and the realized RHCP gain versus frequency of the proposed antenna.

FIGURE 9. Photographs of (a) 7 brass metal layers required to assemble one antenna, (b) microscopic image of the aperture-type FSS layer, and (c) the manufactured assembled antenna mounted on a standard WM-864 waveguide flange. The antenna is aligned using two standard alignment dowel pins and fixated with four plastic screws. The standard flange size is 20 mm × 20 mm.

22.3 GHz covering from 292.2 to 314.5 GHz. The simulated 3-dB RHCP gain bandwidth is 9.7% (from 287 to 316 GHz) of the center frequency with a maximum RHCP gain of 16.1 dBic at 298 GHz.

III. FABRICATION PROCESS

To achieve ease of fabrication, we used the laser cutting brass technology for each metal layer in the proposed antenna using a LPK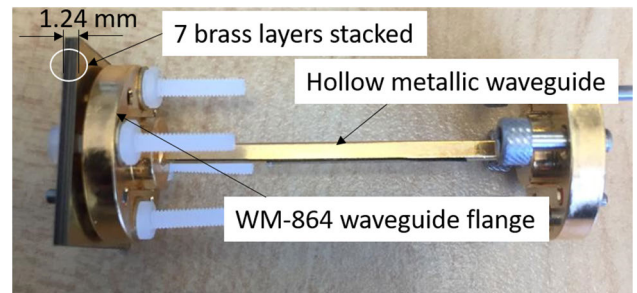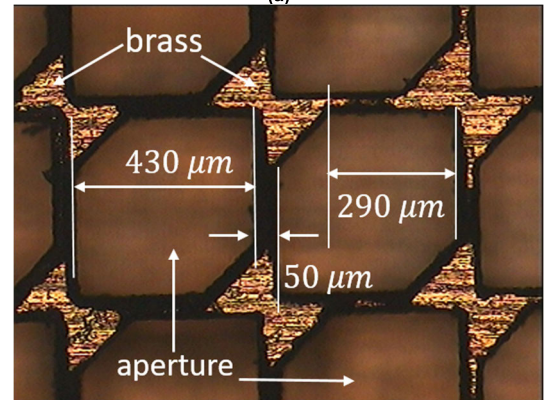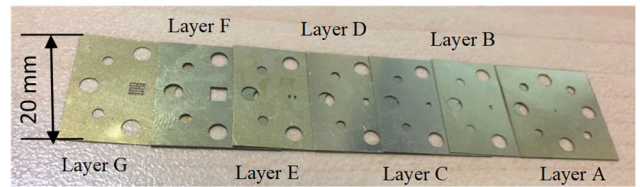F ProtoLaser U4 laser machine with technical support from M2ARS (Ch. Guitton and F. Boutet). The seven brass metal layers needed for one antenna assembly, having different thicknesses as shown in Table 1, have been used to manufacture the proposed 300 GHz CP-FPC antenna as shown in Fig. 9a. These brass materials are often used for laser-cut metals, which are highly reflective materials with an electrical conductivity $\sigma = 35.86 \times 10^6$ Sm^{-1}.

All brass metal layers are fixed by using four plastic screws. The ultraviolet (UV) laser beam ($\lambda = 355$ nm in the UV spectrum) is focused on each brass metal layer separately, having a different thickness in obtaining the desired dimension, with appropriate settings, such as laser cutting speed of 200 mm/s and a laser spot size (i.e., the diameter of the focused laser beam) of 20 μm; which is the fabrication tolerance. Using a metallic layer to form a CP-FPC antenna is advantageous in simplifying its fabrication process based on which the aperture–FSS layer and feeding antenna layers can be fabricated separately then assembled at a later fabrication stage. This reduces the fabrication complexity and
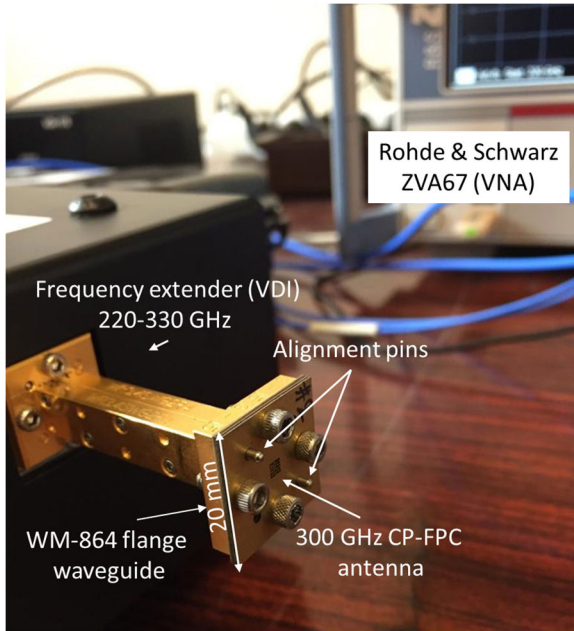
FIGURE 10. Impedance matching measurement setup, where antenna prototype mounted on a standard WM-864 waveguide flange using two alignment pins and four screws.
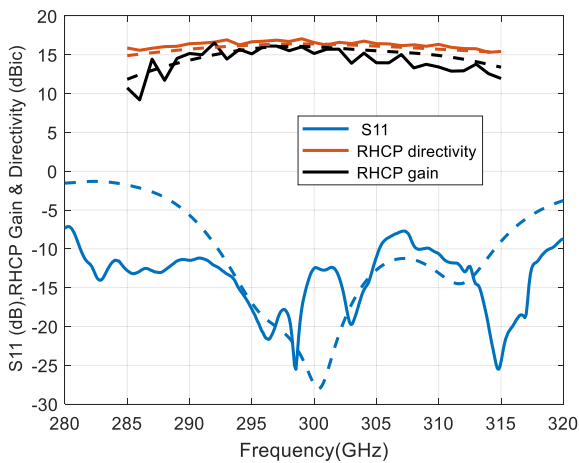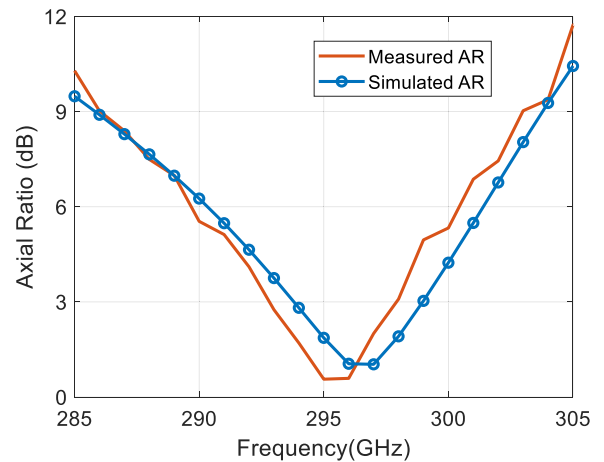

FIGURE 11. Measured (solid lines) and simulated (dashed lines) of reflection coefficient (S11), RHCP realized gain, and RHCP directivity for the 300 GHz CP-FPC antenna prototype.

cost. Fig. 9b shows a microscopic image of the aperture-type FSS layer, where the actual sidewall width was found to be 50 μm. The proposed antenna with periodic aperture–FSS layer is fabricated and assembled, as shown in Fig. 9c. The complete antenna is composed of a feeding antenna parts (A–F layers), 5×5 metallic apertures–FSS part and a standard WM-864 rectangular waveguide with UG-387/U flange.

The metallic layers contain holes for the alignment pins and screws, enabling a direct connection to the standard UG-387 waveguide flange without any additional test fixtures or interfaces. This direct-mount procedure is easier to alternative setups of silicon-micromachining which needs the bonding alignment method [17]. This technology is attractive
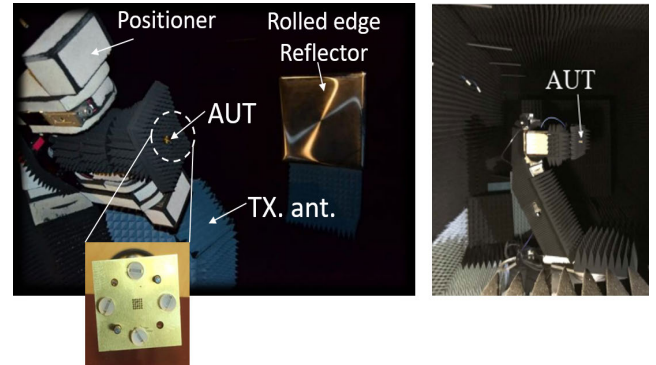
FIGURE 12. The far-field radiation patterns measurement setup at IETR.

FIGURE 13. Axial ratio (AR) (measured and simulated) of the proposed antenna.
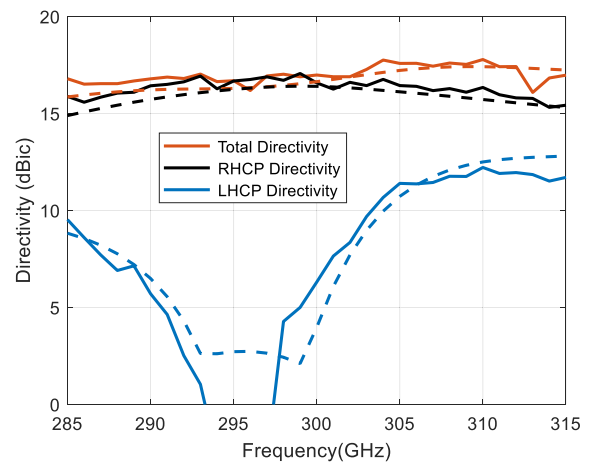
FIGURE 14. Measured (solid lines) and simulated (dashed lines) of the total, RHCP, and LHCP directivities.

in terms of low cost and less complexity compared with silicon micromachining technology.

IV. MEASUREMENT AND RESULTS
In this section, we present the measurements of the fabricated prototype. The reflection coefficient (S11) is measured based

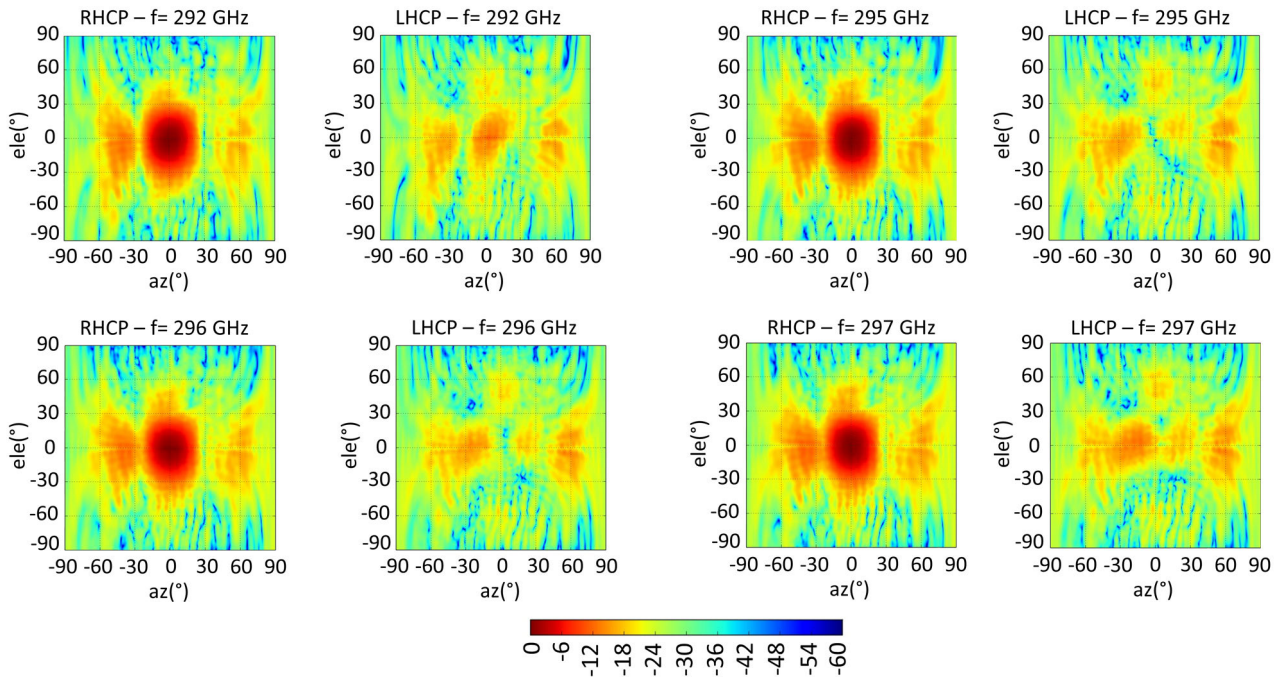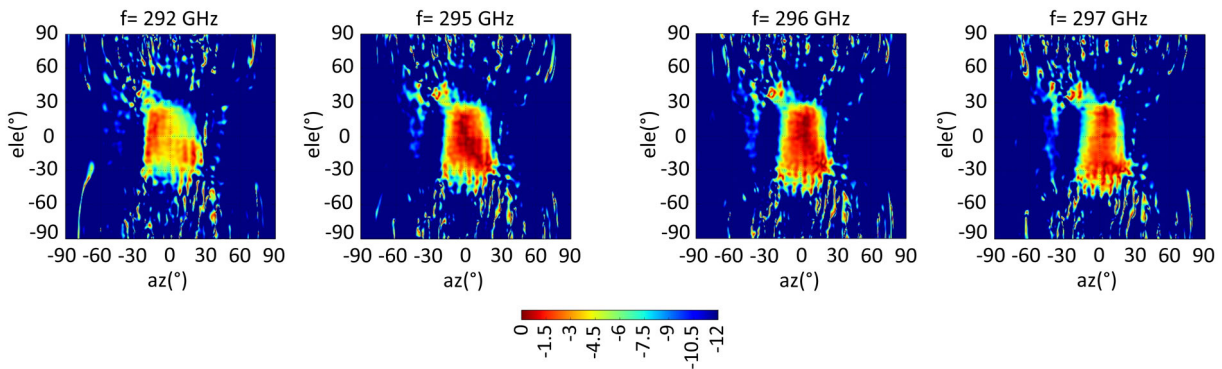**FIGURE 15.** Measured normalized 2D co-polarization (RHCP) and cross-polarization (LHCP) radiation patterns of the proposed antenna at different frequencies. The color bar is on the dB scale.

FIGURE 16. Measured normalized 2D axial ratio plots at 292, 295, 296 and 297 GHz. The color bar is on the dB scale.

on a setup shown in Fig. 10. The basic components of the setup consist of a Rohde & Schwarz ZVA67 vector network analyzer (VNA) and a Virginia Diodes Inc. (VDI) frequency extender module (220 – 330 GHz) with WM-864 waveguide flange interface.

The measured reflection coefficient (S11<–10 dB) is at a working band from 281 to 305 GHz with a bandwidth of 24 GHz, as shown in Fig. 11. Figure. 11 also indicates the measured RCHP gain and RHCP directivity of the CP-FPC antenna and it shows that the RCHP gain of the antenna is 13.4 to 16.5 dBic from 290 to 310 GHz. The antenna yields a maximum measured RHCP gain of 16.5 dBic and a measured RHCP directivity of 16.7 dBic at 292 GHz. There is some divergence between the measured RHCP realized gain and

simulated results; this may be because of assembling and fabrication tolerances that are acceptable in the 300 GHz band.

To demonstrate the proposed antenna's characteristics, such as the axial ratio, realized gain, directivity and half-power beamwidth (HPBW), radiation patterns are measured in a compact-antenna test range (CATR) chamber at IETR (funded by the European Union through the European Regional Development Fund, through the CPER Projects 2015–2020 SOPHIE/STIC and Ondes).

The measurement setup consists of a transmit antenna, a reflector, a positioner, and the antenna under test (AUT). A picture of the setup is shown in Fig. 12.
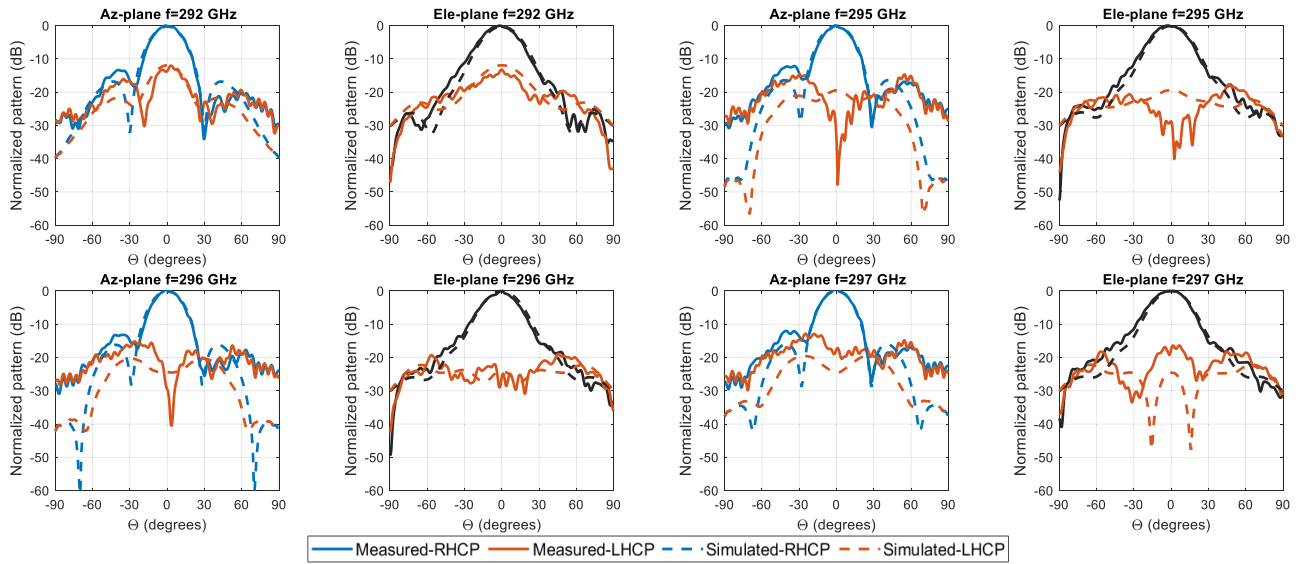
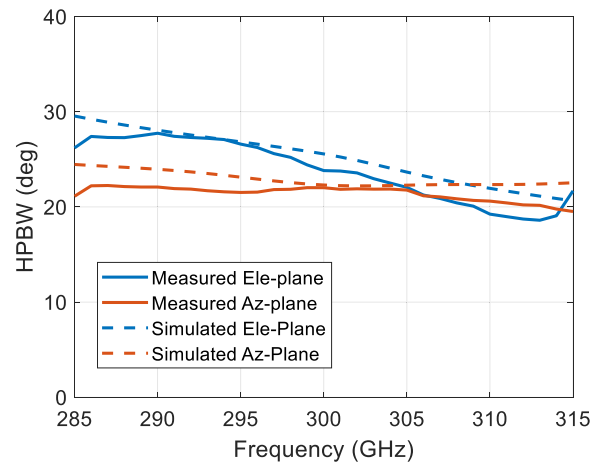**FIGURE 17.** Measured (solid lines) and simulated (dashed lines) broadside radiation patterns of the designed antenna in both principle planes at different frequencies.

The CATR is based on a corner-fed rolled edge reflector of approximately 1200 mm × 1200 mm, producing a cylindrical quiet zone of 600 mm diameter and 600 mm depth. The approximate distances from the feed to reflector and the reflector to the AUT are respectively 2.3 m and 3.8 m. But as the spillover (i.e. radiation from the feed that falls outside the edge of the reflector) is low, the distance between the reflector and the AUT is not the key point for the dynamic range budget. The CATR feed is a 13 dBi linear CATR feed horn designed and manufactured by Thomas Keating Ltd.

The AUT is placed on a roll over slide over azimuth positioner. The CATR feed orientations is obtained using a high precision rotation axis. The whole system is settled in a temperature controlled anechoic chamber of 3.5 m × 3.0 m × 11 m.

The RF measurement system architecture is very classical and is based on VDI WR3 TxRef and high dynamic Rx modules, highlighting a minimum dynamic range of 120 dB. The dynamic range of the whole system is sufficient to have a dataset eligible to the specific calibration procedure developed by IETR [21]. With such calibration, classical computation of the AR using two orthogonal orientations of linear polarization feed is possible. In fact, this calibration enables to estimate and compensate phase error introduced by the positioning system, limiting the phase error to the contributions of the RF measurement system dynamic range.

The AR is computed using a classical procedure based on a complex measurement of the electrical field received by the AUT when two orthogonal orientations of the linearly polarized feed. This computation is possible thanks to our specific calibration procedure of the CATR, enabling as well 3D measurement with Ludwig 3 representation without polarization tracking, and knowledge of the electrical field ellipse of polarization for each sampling points.

FIGURE 18. Measured (solid lines) and simulated (dashed lines) HPBW for the Ele-plane, and Az-plane cuts.

The measured 3-dB AR bandwidth obtained is 5.12 GHz (292.8–297.92 GHz), whereas the simulated one is 5.17 GHz (293.8–298.97 GHz) and is presented in Fig. 13.

The proposed CP-FPC antenna has a measured RHCP directivity of 16 dBic and a 3-dB RHCP directivity bandwidth of 10% (285–315 GHz) over the desired band. The measured 3-dB AR bandwidth is 5.12 GHz (292.8–297.92 GHz), as shown in Fig. 14. The measurement of directivity of the antenna is computed using spherical harmonic expansion tool [21]–[23], which is applied to reconstruct the 3D radiation pattern at any point as it gives access to an exact interpolation of the complex EM electrical field.

The measured 2D-radiation pattern of the proposed antenna for both co-polarization (RHCP) and cross-polarization (LHCP) at different frequencies are presented in Fig. 15. The fabricated prototype works as the RHCP
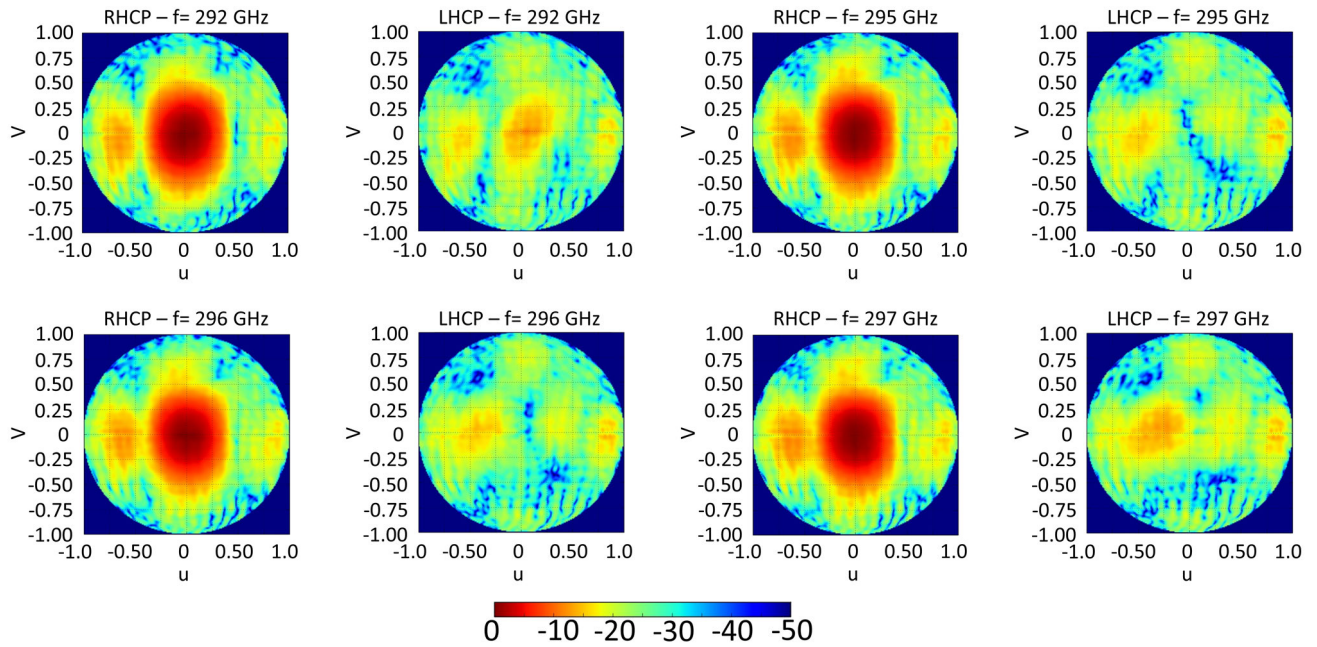
FIGURE 19. Measured 3D-radiation pattern of the proposed antenna (RHCP and LHCP components) in the u−v spectral plane at different frequencies. The color bar is on the dB scale.

TABLE 2. Comparison between the proposed work with other latest cp sub-THz antenna.

| Ref.	Antenna type	Freq (GHz)	3dB-AR BW (%)	Max gain (dBic)	Matching BW (%)	3-dB gain BW (%)	Fabrication process	Fabrication complexity	Size
[16]	Double-fan-shaped slot	495	2	12.5	2	NA	Silicon micromachining	Moderate	$13.3\lambda_0 \times 13.3\lambda_0 \times 1.3\lambda_0$
[13]	Dielectric lens	300	~18.3	30.8	NA	26.66	3D printing	High	$20\lambda_0 \times 20\lambda_0 \times 4.2\lambda_0$
[12]	Conical horn	300	2.33	18.4	20	NA	Wire EDM	Moderate	$4\lambda_0 \times 4\lambda_0 \times 4.1\lambda_0$
[24]	Deflection pyramidal horn	300	33.33	10.4	33.33	13.3	CNC	High	$10\lambda_0 \times 1.5\lambda_0 \times 6.7\lambda_0$
This work	Fabry-Perot cavity	300	1.73	16.5	8	6.66	Laser cutting	Low	$2.6\lambda_0 \times 2.6\lambda_0 \times 1.24\lambda_0$

NA (not available), BW (bandwidth), Freq (Frequency)

antenna from 292 to 297 GHz, confirming the proposed simulated antenna results. It is clear from Fig. 15 that the measured normalized patterns occur at broadside direction, which is equivalent to azimuth (az = 0°) and elevation (ele = 0°).

Fig. 16 shows the 2D measured AR plots of the proposed antenna at 292, 295, 296 and 297 GHz respectively. The AR is kept below 3 dB within the scope of the main beam between −13.2° and 13.2° at broadside direction for the frequencies shown in this figure. The AR reaches a lower value near 0.51 dB at 295 and 296 GHz, as shown in the figure by the black color in the bar in the dB scale.

The normalized measured RHCP (co-pol) and LHCP (cross-pol) radiation patterns of the fabricated antenna in both azimuth-plane and elevation-plane cuts, at four frequency points (292, 295, 296, and 297 GHz), are shown in Fig. 17. There is a good agreement between all simulations and measurement results. Also, there is approximately a 20-dB difference between the co-pol and cross-pol measured gain values (i.e., cross-polarization discrimination (XPD) = 20 dB) at 295 and 296 GHz, similar to the simulated ones.

The CP-FPC antenna has an average measured HPBW in both Ele-plane and Az-plane. The simulated and measured data are shown in Fig. 18, which are in acceptable.
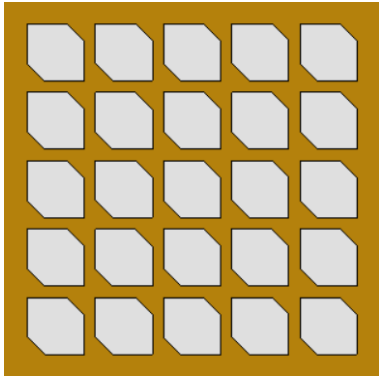
FIGURE 20. Rotation of the hexagonal aperture–FSS layer for LHCP-FPC antenna.

To verify the results and investigate the radiation characteristics outside the two principal planes (Az-plane and Ele-plane), we measured the 3D radiation pattern for the CP-FPC antenna. The results plotted in Fig. 19, show a wide-radiation pattern in the v-plane ($v = \sin\theta\sin\phi$), and a narrow-radiation pattern in the u-plane ($u = \sin\theta\cos\phi$).

It is noticed that the proposed antenna radiates RHCP radiation. The LHCP radiation FPC antenna will be generated easily by rotating the aperture–FSS layer by 90°, as shown in Fig. 20. The LHCP antenna's simulation results are the same as those for the proposed antenna due to their completely symmetric structure, except that the new antenna radiates LHCP waves. This indicates that both RHCP and LHCP FPC antennas can be designed with the proposed hexagonal aperture–FSS layer.

The proposed CP-FPC antenna's performance is compared with other recently reported sub-THz CP antennas, which are summarized in Table 2. Some key parameters are listed, including frequency design, 3dB AR bandwidth, realized gain, and fabrication technology. Table 2 indicates that our proposed antenna delivers high-gain, low-cost, and low-profile structure compared to the others.

V. CONCLUSION

A CP-FPC antenna working in the sub-THz band has been presented. The proposed antenna has been designed with the standard WM-864 waveguide flange dimensions, and it has been fabricated in brass metal using laser cutting technology. The metallic aperture–FSS layer was working as a polarizer to convert LP waves into CP waves. The 300 GHz CP-FPC antenna has been characterized using a millimeter-wave compact range anechoic chamber, obtaining radiation patterns characteristics between the frequency from 285 to 315 GHz. A 3 dB measured AR bandwidth of approximately 1.73 % (5.12 GHz) with a central frequency of 296 GHz is achieved. Finally, it has a low profile of $2.6\,\lambda_0 \times 2.6\,\lambda_0 \times 1.24\,\lambda_0$, which can be applied to future terahertz wireless communication systems in the sub-THz band.

REFERENCES

[1] M. Giordani, M. Polese, M. Mezzavilla, S. Rangan, and M. Zorzi, "Toward 6G networks: Use cases and technologies," *IEEE Commun. Mag.*, vol. 58, no. 3, pp. 55–61, Dec. 2020.

[2] F. Norouzian, E. Marchetti, M. Gashinova, E. Hoare, C. Constantinou, P. Gardner, and M. Cherniakov, "Rain attenuation at millimeter wave and low-THz frequencies," *IEEE Trans. Antennas Propag.*, vol. 68, no. 1, pp. 421–431, Jan. 2020.

[3] H.-J. Song and T. Nagatsuma, "Present and future of terahertz communications," *IEEE Trans. THz Sci. Technol.*, vol. 1, no. 1, pp. 256–263, Sep. 2011.

[4] *IEEE Standard for High Data Rate Wireless Multi-Media Networks–Amendment 2: 100 Gb/s Wireless Switched Point-to-Point Physical Layer*, Standard 802.15.3d-2017 (Amendment to IEEE Std 802.15.3-2016 as amended by IEEE Std 802.15.3e-2017, 2017, pp. 1–55.

[5] N. Llombart, K. B. Cooper, R. J. Dengler, T. Bryllert, and P. H. Siegel, "Confocal ellipsoidal reflector system for a mechanically scanned active terahertz imager," *IEEE Trans. Antennas Propag.*, vol. 58, no. 6, pp. 1834–1841, Jun. 2010.

[6] J. Britton, J. P. Nibarger, K. W. Yoon, J. A. Beall, D. Becker, H. M. Cho, G. C. Hilton, J. Hubmayr, M. D. Niemack, and K. D. Irwin, "Corrugated silicon platelet feed horn array for CMB polarimetry at 150 GHz," *Proc. SPIE*, vol. 7741, Jul. 2010, Art. no. 77410T.

[7] Z. Wu, M. Liang, W.-R. Ng, M. Gehm, and H. Xin, "Terahertz horn antenna based on hollow-core electromagnetic crystal (EMXT) structure," *IEEE Trans. Antennas Propag.*, vol. 60, no. 12, pp. 5557–5563, Dec. 2012.

[8] A. P. Feresidis and J. C. Vardaxoglou, "High gain planar antenna using optimised partially reflective surfaces," *IEE Proc.-Microw., Antennas Propag.*, vol. 148, no. 6, pp. 345–350, Dec. 2001.

[9] B. Aqlan, H. Vettikalladi, and M. A. S. Alkanhal, "Millimeter wave antenna with frequency selective surface (FSS) for 79 GHz automotive radar applications," *Int. J. Microw. Wireless Technol.*, vol. 9, no. 2, pp. 281–290, Mar. 2017.

[10] B. Aqlan, M. Himdi, H. Vettikalladi, and L. Le-Coq, "A 300-GHz low-cost high-gain fully metallic Fabry–Pérot cavity antenna for 6G terahertz wireless communications," *Sci. Rep.*, vol. 11, no. 1, p. 7703, Dec. 2021.

[11] S. Bhardwaj and J. L. Volakis, "Hexagonal waveguide based circularly polarized horn antennas for sub-mm-wave/terahertz band," *IEEE Trans. Antennas Propag.*, vol. 66, no. 7, pp. 3366–3374, Jul. 2018.

[12] B. Aqlan, M. Himdi, L. Le Coq, and H. Vettikalladi, "Sub-thz circularly polarized horn antenna using wire electrical discharge machining for 6G wireless communications," *IEEE Access*, vol. 8, pp. 117245–117252, 2020.

[13] G. B. Wu, Y.-S. Zeng, K. F. Chan, S.-W. Qu, and C. H. Chan, "High-gain circularly polarized lens antenna for terahertz applications," *IEEE Antennas Wireless Propag. Lett.*, vol. 18, no. 5, pp. 921–925, May 2019.

[14] G. Wu, Y. Zeng, K. F. Chan, S. Qu, and C. H. Chan, "3-D printed circularly polarized modified Fresnel lens operating at terahertz frequencies," *IEEE Trans. Antennas Propag.*, vol. 67, no. 7, pp. 4429–4437, Jul. 2019.

[15] Y. Liu, H. Lu, Y. Wu, M. Cui, B. Li, P. Zhao, and X. Lv, "Millimeter-wave and terahertz waveguide-fed circularly polarized antipodal curvedly tapered slot antennas," *IEEE Trans. Antennas Propag.*, vol. 64, no. 5, pp. 1607–1614, May 2016.

[16] P. Zhao, Y. Liu, H. Lu, Y. Wu, and X. Lv, "Experimental realization of terahertz waveguide-fed circularly polarized double-fan-shaped slot antenna," *IEEE Antennas Wireless Propag. Lett.*, vol. 16, pp. 2066–2069, 2017.

[17] A. Gomez-Torrent, U. Shah, and J. Oberhammer, "Compact silicon-micromachined wideband 220–330-GHz turnstile orthomode transducer," *IEEE Trans. THz Sci. Technol.*, vol. 9, no. 1, pp. 38–46, Jan. 2019.

[18] G. Von Trentini, "Partially reflecting sheet arrays," *IRE Trans. Antennas Propag.*, vol. 4, no. 4, pp. 666–671, Oct. 1956.

[19] D. R. Jackson and A. A. Oliner, "A leaky-wave analysis of the high-gain printed antenna configuration," *IEEE Trans. Antennas Propag.*, vol. 36, no. 7, pp. 905–910, Jul. 1988.

[20] A. Foroozesh and L. Shafai, "Investigation into the effects of the patch-type FSS superstrate on the high-gain cavity resonance antenna design," *IEEE Trans. Antennas Propag.*, vol. 58, no. 2, pp. 258–270, Feb. 2010.

[21] L. Le Coq, N. Mézières, P. Leroy, and B. Fuchs, "Some contributions for antenna 3D far field characterization at terahertz," *Sensors*, vol. 21, no. 4, p. 1438, Feb. 2021.

[22] N. Mézières, B. Fuchs, L. Le Coq, J.-M. Lerat, R. Contreres, and G. Le Fur, "On the application of sparse spherical harmonic expansion for fast antenna far-field measurements," *IEEE Antennas Wireless Propag. Lett.*, vol. 19, no. 5, pp. 746–750, May 2020.

[23] N. Mezieres, B. Fuchs, L. Le Coq, J.-M. Lerat, R. Contreres, and G. Le Fur, "On the antenna position to improve the radiation pattern characterization," *IEEE Trans. Antennas Propag.*, early access, Mar. 2, 2021, doi: 10.1109/TAP.2021.3060894.

[24] H. Yu, J. Yu, Y. Yao, X. Liu, and X. Chen, "Wideband circularly polarised horn antenna with large aspect ratio for terahertz applications," *Electron. Lett.*, vol. 56, no. 1, pp. 11–13, Jan. 2020.

HAMSAKUTTY VETTIKALLADI received the Ph.D. degree from Cochin University of Science and Technology, and the Habilitation A Diriger des Recherches degree from the University of Rennes 1, France, in 2018. He started his carrier as a Postdoctoral Researcher with the Bell Engineering Department, University of Arkansas, USA, in January 2008, just after finishing his Ph.D. degree. From September 2008 to November 2012, he was working as a Postdoctoral Fellow with the Institute of Electronics and Telecommunication of Rennes, University of Rennes 1. From November 2012 to December 2017, he was an Assistant Professor with King Saud University. Since January 2018, he has been an Associate Professor with the Department of Electrical Engineering, King Saud University. He is the author of more than 85 scientific publications in international journals and conferences and three book chapter. His main research interests include microwave, millimeter and THz antenna design for various applications, including high-speed WIFI, automotive radar, imaging, point to point communication, and 5G. He has served as a Visiting Faculty in several institutes, as an editor and a referee in several scientific journals and conferences.

BASEM AQLAN received the master's degree in electrical engineering from King Saud University, Riyadh, Saudi Arabia, in 2016. He is currently pursuing the Ph.D. degree in signal processing and telecommunications from the University of Rennes 1, France. Since 2012, he has been a Researcher with King Saud University. His research interests include millimeter wave and THz antennas design for various applications, including high-speed WIFI, 79-GHz automotive radar, and beyond 5G/6G cellular wireless communication.

MOHAMED HIMDI received the Ph.D. degree in signal processing and telecommunications from the University of Rennes 1, France in 1990. Since 2003, he has been a Professor with the University of Rennes 1, and the Head of the High Frequency and Antenna Department, IETR, in 2013. He has authored or coauthored 133 journal articles and over 280 papers in conference proceedings. He has also coauthored nine book chapters. He holds 40 patents. His research activities concern passive and active millimeter-wave antennas. His research interests include development of new architectures of antenna arrays, and new three-dimensional (3-D) antenna technologies. He was a Laureate of the 2d National Competition for the Creation of Enterprises in Innovative Technologies, in 2000 (Ministry of Industry and Education). He received the JEC-AWARD at Paris on Pure Composite Material Antenna Embedded into a Motorhome Roof for the Digital Terrestrial Television Reception in March 2015.

LAURENT LE-COQ received the electronic engineering and radio communications degree and the French DEA (M.Sc.) degree in electronics from the National Institute of Applied Science (INSA), Rennes, France, in 1995, and the Ph.D. degree from the National Institute of Applied Science (INSA) in 1999. He joined the Institute of Electronics and Telecommunications of Rennes (IETR), University of Rennes 1, as a Research Laboratory Engineer, in 1999, responsible of antenna centi- and milli-meter wave range test facilities. Since 2018, he has been the Scientific Manager of Manufacturing Measurement and Analysis of Radiating Systems (M2ARS), the IETR facility unit bringing together seven facilities dedicated to electromagnetic studies up to 500-GHz, among which three antenna test and imaging facilities (up to 300-GHz) and a prototyping service. His activities in antenna measurements and development of related procedures involved him in more than 30 research contracts of national or European interest. He is the author or coauthor of more than 50 journal articles and 50 papers in conference proceedings.

• • •